Low Dose Scanning Transmission Electron Microscopy of Organic Crystals by Scanning Moiré Fringes

Mark S'ari[1,*], James Cattle[1], Nicole Hondow[1], Rik Brydson[1], Andy Brown[1]

School of Chemical and Process Engineering, University of Leeds, Leeds LS2 9JT, United Kingdom

Abstract

In the pharmaceutical industry, it is important to determine the effects of crystallisation and processes, such as milling, on the generation of crystalline defects in formulated products. Conventional transmission electron microscopy and scanning transmission electron microscopy (STEM) can be used to obtain information on length scales unobtainable by other techniques, however, organic crystals are extremely susceptible to electron beam damage. This work demonstrates a bright field (BF) STEM method that can increase the information content per unit specimen damage by the use of scanning moiré fringes (SMFs). SMF imaging essentially provides a magnification of the crystal lattice through the interference between closely aligned lattice fringes and a scanning lattice of similar spacing. The generation of SMFs is shown for three different organic crystals with varying electron beam sensitivity, theophylline, furosemide and felodipine. The electron fluence used to acquire the BF-STEM for the most sensitive material, felodipine was approximately 3.5 $e^-/Å^2$. After one additional scan of felodipine (total fluence of approximately 7.0 $e^-/Å^2$), the SMFs were no longer visible due to extensive damage caused to the crystal. Irregularity in the SMFs suggested the presence of defects in all the organic crystals. Further effort is required to improve the data analysis and interpretation of the resulting SMF images, allowing more information regarding the crystal structure and defects to be extracted.

Keywords:
Low dose, Bright field STEM, Organic crystals, Scanning moiré fringes, Dose-limited resolution

1. Introduction

Scanning transmission electron microscopy (STEM) is a powerful characterisation technique and has been used to provide high-resolution information at length scales of < 0.5 Å in spherical aberration-corrected STEMs [1]. To achieve such high-resolution it is necessary for the current density in a sub-Ångström sized probe to provide sufficient current to produce an adequate signal-to-noise ratio. This is particularly important for techniques such as high-angle annular dark field imaging where only a fraction

*Corresponding Author
Email address: M.S.S'ari@leeds.ac.uk (Mark S'ari)

of the scattered electrons are collected. However, as a consequence of the high current densities, samples must be able to resist large amounts of electron radiation, typically $> 10^5$ - 10^6 $e^-/Å^2$.

In general, inorganic materials such as metals and metal oxides are electron beam stable under these conditions whilst biological materials, inorganic-organic hybrid materials and organic crystals (including polymers and small molecules) are more easily damaged. The electron beam sensitivity of a material can be quantified by measuring the critical electron fluence (C_F) [2]. This is calculated by measuring the intensity of a feature, such as electron diffraction spots and determining the electron fluence at which the maximum intensity drops to e^{-1} during exposure to the electron beam. For irradiation energies of 80 - 300 kV, biological materials typically have C_F values in the range of 1 - 15 $e^-/Å^2$, organic crystals 0.2 - 120 $e^-/Å^2$, zeolites 100 - 600 $e^-/Å^2$ and transition metal oxides $> 10^7$ $e^-/Å^2$ [3, 4, 5, 6, 7, 8].

The mechanism by which a material is damaged by the electron beam can be categorised by the type of electron scattering, either elastic scattering, inelastic scattering or a combination of both [9]. Depending on the most prevalent mechanism different experimental conditions can be adapted to improve the C_F [10]. For insulating materials such as organic crystals and biological materials radiolysis resulting from inelastic electron scattering is the main mechanism for damage [9]. Two experimental factors that affect the amount or degree of radiolysis that occurs are accelerating voltage (kV) and temperature. An increase in kV decreases the damage rate to the sample due to an inverse relationship between the inelastic scattering cross-section and kV [11, 12]. Cryogenic temperatures improve C_F by reducing the mobility of highly reactive damaged fragments, increasing stability by a factor of 1 - 10 compared to room temperature, and cryo-TEM is routinely used to examine biological samples [13, 14, 15]. In addition, the chemical structure has an effect on the electron beam stability with conjugated compounds being more stable as compared to aliphatic compounds [16, 17]. The relationship between chemical structure and C_F has been investigated for poorly water-soluble drugs and compounds with a higher ratio of conjugated carbons as compared to non-conjugated carbons tended to be more stable whilst the presence of hydrogen bonds acceptors and donors negatively influenced C_F [18].

For the pharmaceutical industry obtaining crystal lattice resolution images of organic compounds can provide important information on the effects of formulation processing on drug properties. For example milling can introduce defects into crystalline active pharmaceutical ingredients (APIs). Crystal defects in APIs are known to be sites at which polymorphic transformations and hydrate formation are initiated, resulting in a significant change to the solid-state behaviour of a API [19, 20, 21].

Previous electron microscopy studies have successfully employed low-dose techniques to achieve lattice and molecular information on beam sensitive materials using conventional transmission electron microscopy (CTEM) with images recorded on photographic film, for example, copper and platinum phthalocyanine, quaterrylene, paraffin and polyethene crystals [5, 22, 23, 24, 25]. More recently CTEM has been used to obtain lattice information of caffeine-glutaric acid co-crystals [26].

To date, few if any high-resolution images of highly beam sensitive materials have been acquired using STEM. One technique that has been used to obtain low-dose STEM images is compressive sensing [27, 28]. This uses the concept that data can be represented in a sparse form and by recording a sub-sampled image the missing data can then be recovered using mathematical algorithms [29, 30]. By sampling fewer pixels this decreases the overall electron fluence that the sample is exposed to.

Another technique that has been used to obtain high-resolution lattice information at a reduced electron fluence in CTEM and STEM are moiré[1] fringes [31]. Moiré fringes arise due to the interference pattern created between a crystal lattice and a similarly sized reference lattice. The resulting interference pattern effectively magnifies the crystal lattice and allows it to be viewed indirectly at lower magnifications and electron fluences than would normally be required. This technique has previously been used in CTEM on polyethene and diamond to analyse the nature of crystalline defects [23, 32, 33]. In the case of STEM, the scanning of the electron beam across the sample creates an artificial lattice which is used as the reference to form scanning moiré fringes (SMFs). Generally, SMFs have been used to analyse large area strain measurements in semiconductors and functional oxides [31, 34, 35, 36, 37, 38]. Additionally, X-ray and core energy loss elemental images of the atomic structure of aquamarine, a beam sensitive mineral, have also been recorded using SMFs [39, 40].

In this study, the effects of pixel size and relative angle on the size of the measured SMFs in bright field (BF) STEM are determined using a form of asbestos, that is relatively stable under the electron beam. This information is then used to examine three highly beam sensitive organic crystals, theophylline furosemide and felodipine. All of which have varying electron beam stabilities. Using SMFs lattice information regarding the presence of defects are obtained. The use of this method to increase the resolution when examining organic crystals in BF-STEM and the application to employ SMFs as a method to examine active pharmaceutical ingredients before and after processing are then discussed.

2. Materials and Methods

2.1. Materials and Operating Conditions

Preliminary studies on crocidolite (one of six mineral forms of asbestos and considered here to be electron beam stable) were carried out to investigate the effects of pixel size and scan rotation on the measured SMFs. Crocidolite was acquired from Agar Scientific Ltd and is used as a standard TEM test sample. Three electron beam sensitive organic crystals were then examined: theophylline, furosemide and felodipine. The critical electron fluence (C_F) of theophylline, furosemide and felodipine have been measured in two previous studies using a microscope operated at 200 kV accelerating voltage and room temperature and were found to be 27.0 $\pm$ 5.0 $e^-/Å^2$, 7.1 $\pm$ 4.0 $e^-/Å^2$ and 2.1 $\pm$ 0.9 $e^-/Å^2$ respectively [18, 41]. C_F increases at higher accelerating voltages, for example, the C_F of theophylline at 300 kV has previously been

[1] interestingly moirés are not named after a person but comes from the French adjective moiré, derived from the verb moirer and earlier mouaire meaning "to produce a watered textile by weaving or pressing". Mouaire was adopted from the English word mohair, which is a cloth made from the wool of the Angora goat.

measured to be 41.0 ± 5.0 $e^-/Å^2$, an improvement of approximately 1.5 times over that at 200 kV [11, 42].

Theophylline was prepared for TEM analysis by drop-casting a theophylline saturated nitromethane solution onto a holey carbon coated copper TEM grid. This formed predominately plate-like crystals of form II theophylline with the [100] zone axis orientated parallel to the electron beam. Furosemide and felodipine were provided by AstraZeneca and prepared by dispersing the powder in water and drop casting the suspended powder onto carbon coated copper TEM grids.

All samples were examined in an FEI Titan^3 Themis G2 operated at an accelerating voltage of 300 kV, equipped with a field emission gun (X-FEG) operating at an extraction voltage of 4.5 kV and a monochromator. The images and diffraction patterns were captured using a Gatan OneView CCD and SMFs using the FEI BF-STEM detector. For a non-aberration corrected STEM, phase contrast is optimised when the collection semi-angle of the bright field disc detector is half of the probe convergence semi-angle [43]. Here the convergence semi-angle is 10 mrad and the collection angle was set to 5.5 mrad. The electron beam current was reduced to mitigate beam-induced damage for the organic crystals by adjusting the monochromator focusing lens and the C2 condenser lens to provide an electron flux of approximately 0.1 $e^-/(Å^2\ s)$ in CTEM. In STEM the electron fluence was controlled by reducing the probe current (I) to 5 ± 2 pA using the monochromator focusing lens and pixel dwell times (t) of 10 μs. The measured probe current was based on a flu-cam current reading which had been calibrated by a Faraday cup. Equation 1 was used to calculate the electron fluence per pixel in STEM and is equivalent to the electron fluence per frame.

$$F(e^-/Å^2) = \frac{I \times t}{e \times d_s^2} \tag{1}$$

where e is the electronic charge of an electron (1.602×10^{-19} C) and d_s is the pixel size which is determined by the selected magnification.

2.2. Scanning Moiré Fringes (SMFs)

Moiré fringes occur due to the interference patterns produced by overlaying two similar, but non-identical lattices. The difference between the lattices can be due to either size, rotation or a combination of both. In the case of STEM, SMFs can be formed via interference between the artificial scanned lattice produced by rastering the electron probe in STEM (d_s) and the real space lattice of the crystal being imaged (d_l). An example of two different types of moiré fringes: translational and general, are shown in Figure 1.

The size of the observed SMFs are dependent on three factors: the magnification in STEM which determines the pixel size and therefore d_s and can only take discrete values, the size of d_l which is determined by the d-spacings within the crystal being imaged and finally the relative angle (β) between fringes of d_s and d_l [31]. If β is equal to zero the overlaid lattices will form translational moiré fringes (d_{TM}), the size of which can be calculated from Equation 2 [44, 45].

$$d_{TM} = \frac{d_s d_l}{|d_s - d_l|} \tag{2}$$

As the ratio between d_s and d_l approaches one, the size of the resulting SMFs tends toward infinity (Figure 2a). When the ratio

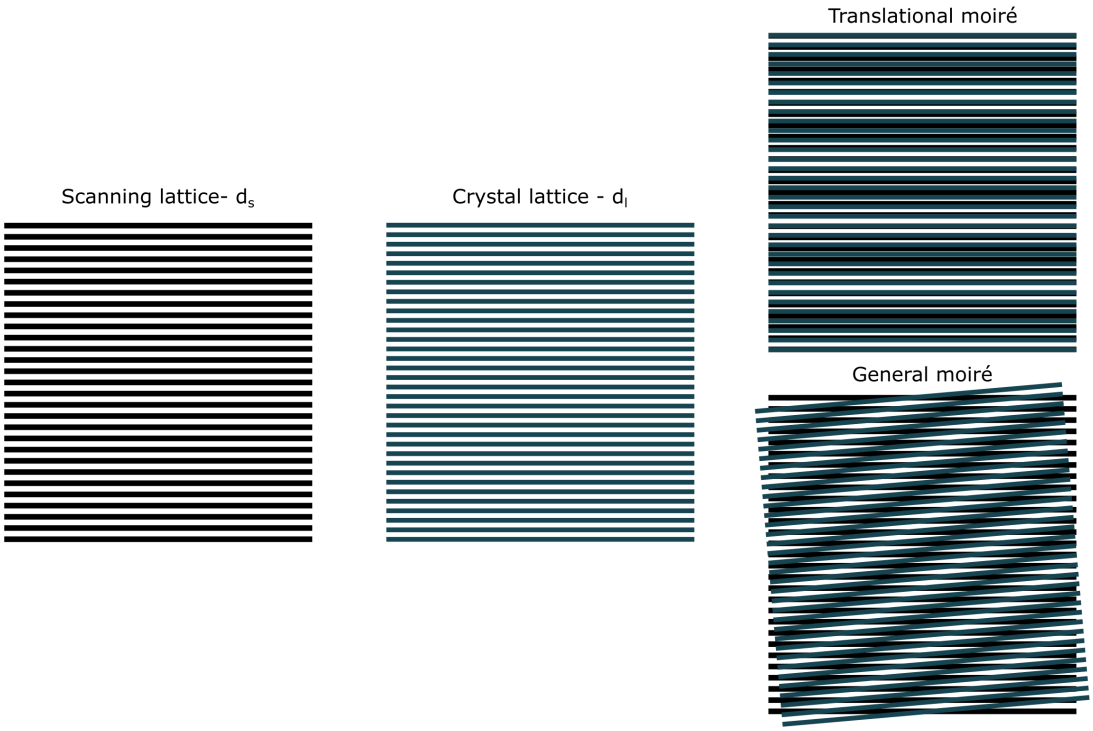

Figure 1: Schematic of translational and general moiré fringes created by a scanning lattice (d_s) and crystal lattice (d_l) of similar sizes. In both moiré fringe images $d_s/d_l = 1.18$ and for the general moiré fringe image $\beta = 5°$.

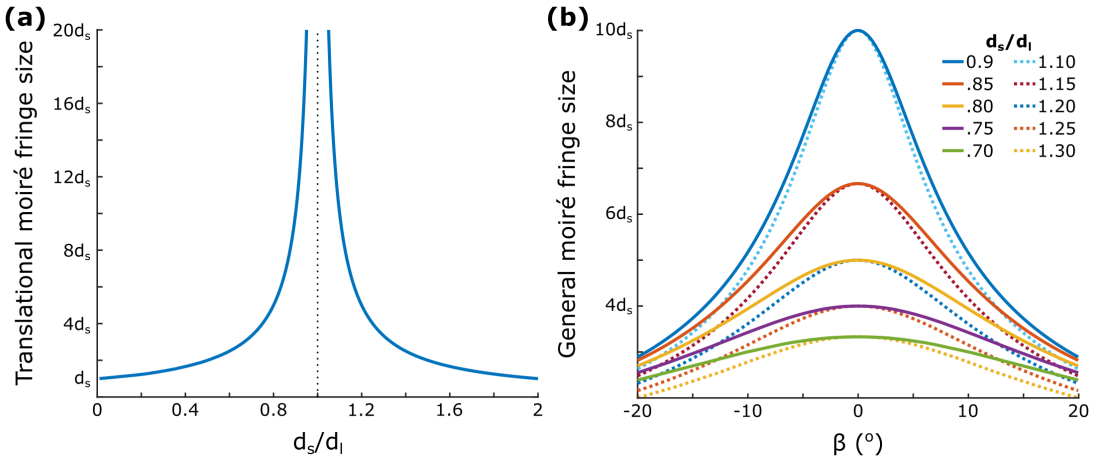

Figure 2: Plots of moiré fringe size at different ratios of d_s and d_l for (a) translational moiré and (b) general moirés.

between d_s and d_l deviates away from one the size of the resulting fringes decrease and are eventually unobservable. If there is an angle β between d_s and d_l, general moiré fringes (d_{GM}) are formed, the size of which can be calculated using Equation 3 [44, 45].

$$d_{GM} = \frac{d_s d_l}{\sqrt{(d_s - d_l)^2 + d_s d_l \beta^2}} \qquad (3)$$

The additional term in the denominator accounts for the rotation between the fringes and as β increases the resulting fringes will decrease in size. Figure 2b shows how the size of the moiré fringes changes with β at different ratios of d_s to d_l.

Table 1: Magnification and respective pixel size and electron fluence when 5 ± 2 pA probe current and 10μs dwell time are used in STEM.

Magnification (× 1/1000)	**Pixel Size (nm)**	**Electron Fluence ($e^-/Å^2$)**
26	3.73	0.2 ± 0.1
74	1.32	1.8 ± 0.7
105	0.93	3.6 ± 1.4
148	0.66	7.2 ± 2.9
210	0.47	14.1 ± 5.7
297	0.33	28.7 ± 11.5
419	0.23	59.1 ± 23.6
593	0.17	108.1 ± 43.3
845	0.16	122.1 ± 48.8

2.3. Data Collection

To acquire translational SMFs β has to be close or equal to zero. Therefore, before acquiring SMFs the scan direction is rotated to align d_s to d_l, by identifying the rotation required from a measurement of a selected area electron diffraction pattern (SAED) of the crystal recorded in CTEM. This includes accounting for the difference in the rotation of alignments between the CCD in CTEM and the BF-STEM detector, which was calculated by measuring the angle of a selected spacing in the SAED pattern and determining the change in rotation compared to the same spacing in an FFT of a high-resolution BF-STEM image.

Very low fluence BF-CTEM was used to identify areas that contained strongly diffracting crystal regions by searching different areas on the grid with a 30 mrad diameter objective aperture inserted. Once an area was identified a SAED pattern was acquired and used to calculate the scan rotation required. The microscope was then operated in STEM and focused (by a Ronchigram) using a sacrificial area of the sample or on the carbon film immediately adjacent to a particle of interest. This step was carried out at a lower magnification than required to obtain SMFs, to limit the total electron fluence. The magnification was then increased and a BF-STEM image containing SMFs was captured. The magnification (and therefore d_s) selected depended on the electron beam sensitivity of the organic crystal and the size of d_l. Table 1 shows the possible magnifications and the respective pixel size and electron fluence calculated when a 5 ± 2 pA probe current and 10 μs pixel dwell time is used.

Prior knowledge of the crystal lattice spacings in the sample is not necessary as the d_l is measured from the SAED and the d_s used then depends on the value of d_l and the electron beam sensitivity of the sample. However, knowing the lattice spacings ahead of time can prevent examining a sample that contains no crystal lattice spacings close enough to the fixed values of d_s available in the microscope resulting in SMFs that are too small to identify.

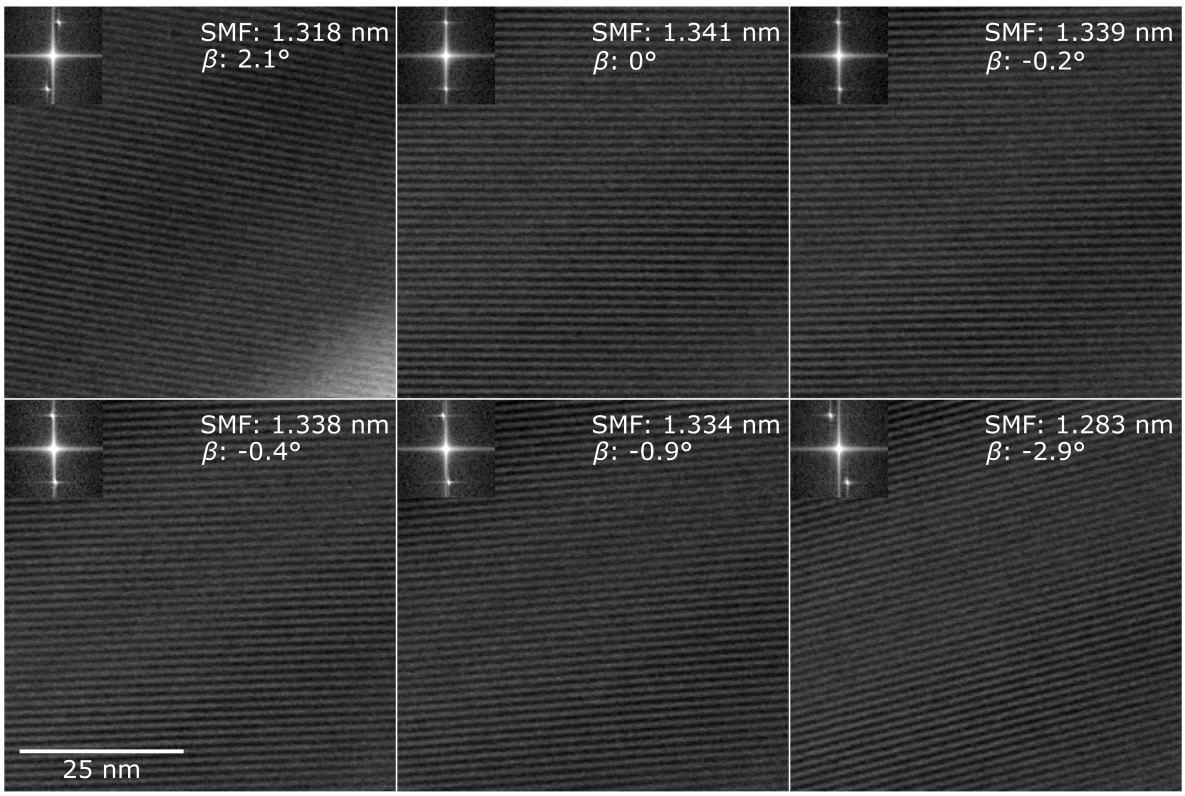

Figure 3: Effect of scan rotation in STEM on the size of the observed moiré fringes of crocidolite; the FFT is shown as an insert for each image and was used to measure the size of the SMFs. The angle β between d_l and d_s and SMF size are displayed for each image; the d_l and d_s were equal to 0.282 $\pm$ 0.002 nm and 0.233 nm respectively.

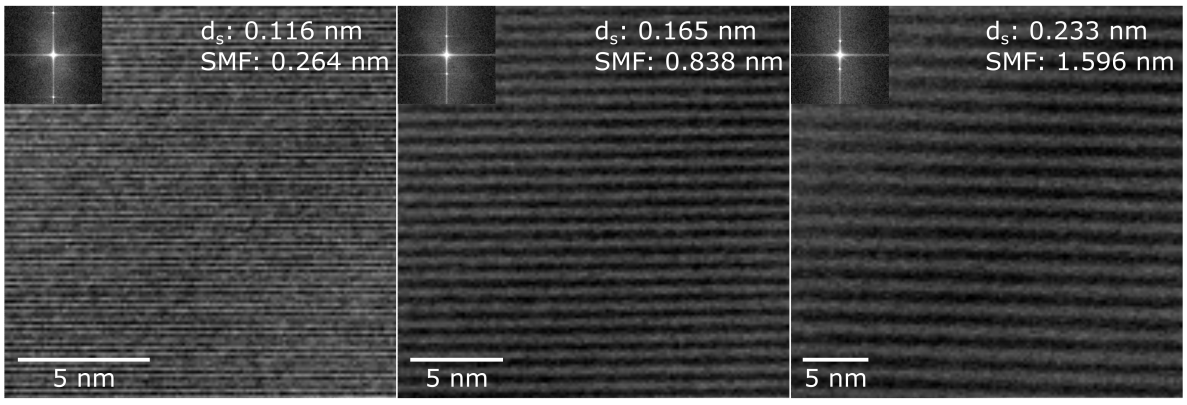

Figure 4: Effect of d_s on the size of the observed SMFs for d_l of 0.203 $\pm$ 0.002 nm of crocidolite; the FFT is shown as an insert for each image and was used to measure the size of the SMFs. The d_s and SMF size are displayed for each image and the scan direction was adjusted so that β was close to zero.

3. Results and Discussion

3.1. Crocidolite

Preliminary results on crocidolite were used to investigate the effect of pixel size (d_s) and scan rotation (β) on the measured SMFs size (Figures 3 and 4 respectively). Due to the high electron beam stability of crocodilite a probe current of 40 ± 2 pA and dwell times of 20 μs were used to capture the images, resulting in an electron fluence per frame of 920 ± 45 $e^-/Å^2$, 1840 ± 90 $e^-/Å^2$ and 3720 ± 190 $e^-/Å^2$ at d_s of 0.233 nm, 0.165 nm and 0.116 nm respectively. Figure 3 displays a collection of SMF images that are a result of the interference between a d_l of 0.282 ± 0.002 nm and d_s of 0.233 nm. The angle β was varied between 2.1° and -2.9° and the resulting size of each SMF was measured via the FFT (shown for each image). As expected the largest SMF spacing was found when β was nominally zero and was measured to be 1.341 ± 0.020 nm. The smallest SMF spacing was measured at 1.283 ± 0.020 nm and was found when β was equal to -2.9°, this being the highest rotation away from zero.

Figure 4 displays a series of SMF images that were a result of the interference between a d_l of 0.203 ± 0.002 nm and various d_s values, these being 0.116 nm, 0.165 nm and 0.233 nm, corresponding to magnifications of 845k, 593k, 419k times respectively. The scan direction for each image was adjusted so that β was close or equal to zero. From these images, the largest SMF was measured at 1.596 ± 0.031 nm and found using a d_s of 0.233 nm, the smallest deviation from d_l (0.203 ± 0.002 nm). When using a d_s of 0.116 nm the measured SMF spacing was only 0.264 ± 0.002 nm and are difficult to identify in the image as they are only 2 - 3 pixels in size, however, from the FFT distinct spacings can be seen.

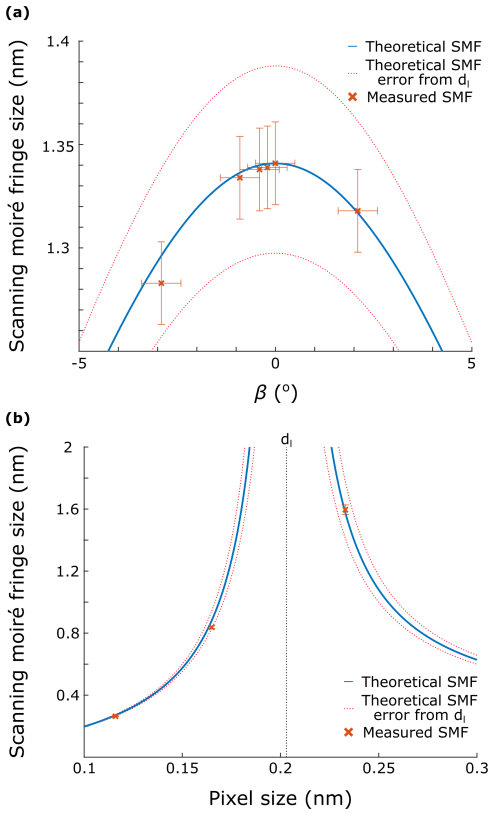

Figure 5: Plots showing the comparison between the measured and calculated size of the SMFs as a function of: (a) rotation angle, β, calculated from Equation 3 and (b) STEM pixel size (d_s), calculated from Equation 2. The red dotted lines show the error in the theoretical value due to the measurement of d_l.

Using Equation 3, the predicted size of the SMF as a function of β (including the error in the measurement of d_l) was calculated and is shown in Figure 5a. For each β value in Figure 3 the size of the measured SMFs were plotted and demonstrate a good agreement to the predicted values. The theoretical curve shows that small variations in β when close to zero (± 1°) have a relatively small effect on the size of the SMFs, however, as the angle deviates further from zero then the SMF spacing begins to decrease.

If the graph was extended beyond 5° then the size of the SMFs would decrease significantly as previously shown in Figure 2b.

Similarly, Figure 5b shows the theoretical size of translational moiré fringes as a function of STEM pixel size (d_s) calculated using Equation 2. For each d_s used in Figure 4 the corresponding measured SMFs were plotted and showed good agreement to the predicted values. The theoretical curve shows that as the ratio between d_s and d_l approaches one (shown by the dotted line) the size of the SMFs dramatically increases; tending towards infinity when $d_s = d_l$. Therefore, when d_s is very similar to d_l small measurement errors may lead to large discrepancies between measured and predicted values.

3.2. Theophylline

Scanning moiré fringes of theophylline form II were acquired by firstly taking a SAED pattern along the [100] zone axis in CTEM (Figure 6a) and then rotating the scan direction to align with the (011) crystal spacing of 0.34 ± 0.02 nm. The pixel size closest to this d-spacing, which would result in the largest SMFs, was 0.33 nm at 225k times magnification. Figure 6b shows the resulting SMFs with a β close or equal to 0. From the spacings measured in the FFT, the average size of the SMFs was found to be 3.90 ± 0.05 nm. The electron fluence used to take a single image in STEM at this magnification was approximately 28.8 $e^-/Å^2$, less than the critical fluence measured via CTEM at 300 kV (41.0 ± 5.0 $e^-/Å^2$). However, the total electron fluence that the crystal was exposed to in this process would be greater than 28.8 $e^-/Å^2$ due to searching for areas in CTEM and recording SAED patterns.

A BF-STEM image of a different crystal area was taken using the same d_s and d_l and Fourier filtered by masking all spatial frequencies in the FFT except the ones relating to the SMFs, shown in Figure 6c. In this case, the resulting SMFs were 2.76 ± 0.03 nm. Compared to the interference bands from the SMFs seen in Figure 6b, additional fringes that appear as terminating half lines are observable within Figure 6c, highlighted by the red lines. These areas cause adjacent fringes to bend to compensate, affecting the average size of the SMF measured via the FFT and cause the spots to become more diffuse. Visibly these areas appear similar to edge dislocations imaged by high-resolution CTEM but are magnified here by the SMF, however, due to β not being 0 the exact interpretation of what defect type this represents in the real space lattice and the direction that they occur is difficult to determine.

3.3. Furosemide

Figure 7a shows the [110] zone axis of furosemide form I with the (001) crystal spacing (1.50 ± 0.10 nm). The scan direction was aligned with this d-spacing and a BF-STEM image recorded at a magnification of 57k times resulted in a d_s of 1.32 nm. Due to the large size of the (001) spacing and the lower magnification required to produce SMFs the fluence per scan was approximately 1.8 $e^-/Å^2$, almost four times lower than the C_F of 7.1 $e^-/Å^2$ previously measured at 200 kV [18]. This allowed for several images to be captured to determine if β was 0 ± 1° and also to more accurately focus the image.

Figure 7b was taken after a cumulative electron fluence of approximately 17.3 $e^-/Å^2$ and contains an image of the entire particle. An FFT of the area highlighted

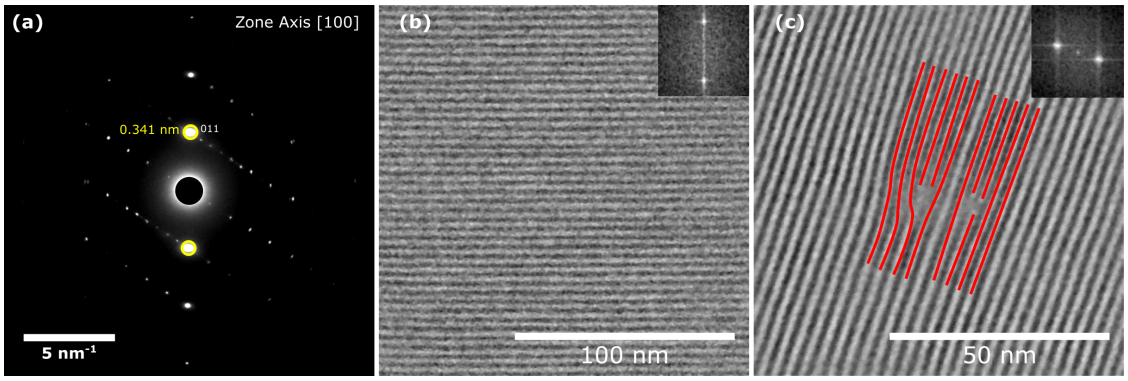

Figure 6: Scanning moiré fringes of theophylline form II (a) SAED of [100] zone axis, the scan direction was aligned with the (011) reflection (0.341 ± 0.020 nm). (b) BF-STEM of the SMFs acquired using a pixel size of 0.33 nm and 0.34 ± 0.02 nm d-spacing, from the FFT the average size of the SMFs were measured at 3.90 ± 0.05 nm. (c) Fourier filtered images of a different crystal area showing a disruption in the SMFs from the 0.34 ± 0.02 nm d-spacing and pixel size of 0.33 nm. The electron fluence used to acquire each image in (b) and (c) was a minimum of 28.8 $e^-/Å^2$.

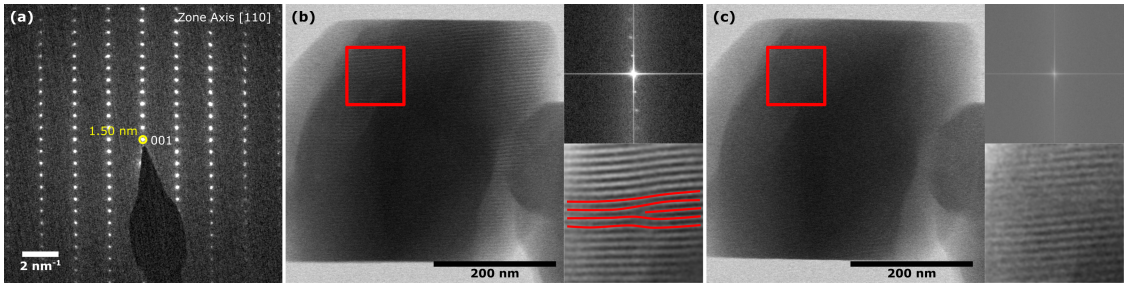

Figure 7: Scanning moiré fringes of furosemide form I (a) SAED of [110] zone axis, the scan direction was aligned with the (001) reflection (1.50 ± 0.10 nm). (b) BF-STEM image of SMFs produced by using a pixel size of 1.32 nm and 1.50 ± 0.10 nm d-spacing. From the FFT the average size of the SMFs was measured at 9.95 ± 0.15 nm. Fourier filtered image from within the red box highlights a defect seen within the crystal. (c) BF-STEM of the same area after an additional electron fluence of 25.5 $e^-/Å^2$. The cumulative electron fluence from STEM in (b) and (c) were approximately equal to 17.3 $e^-/Å^2$ and 42.8 $e^-/Å^2$ respectively.

in the red box and a Fourier filtered image of the same area are also shown. The average size of the first order spacings measured from the FFT was equal to 9.95 ± 0.15 nm. Similar to the case of theophylline from the Fourier filtered image an extra terminating fringe can be identified causing the surrounding fringes to bend. In this case, however, the angle β is close or equal to zero and this disruption to the regular moiré fringe pattern may be due to a lattice defect such as a dislocation in the same orientation shown in the image. Figure 7c shows the point at which the crystal was sufficiently damaged and spots were no longer visible in the FFT; fringes can still be seen in the Fourier filtered image, however, these are artefacts due to applying the spatial filter.

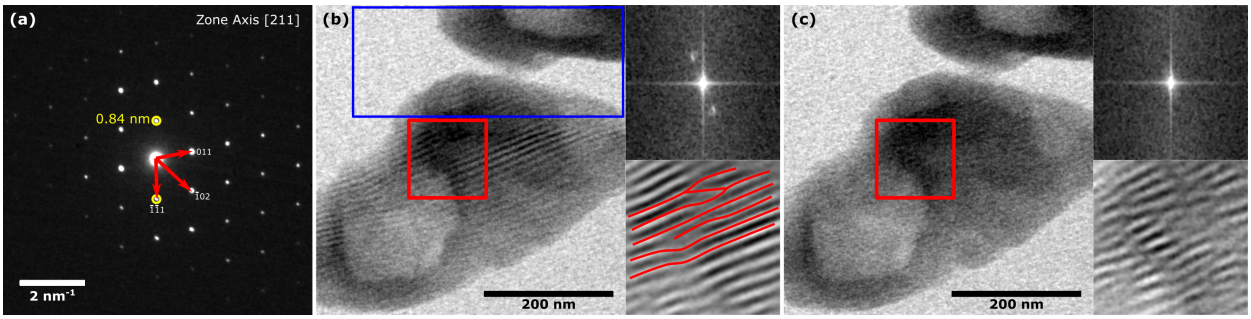

Figure 8: Scanning moiré fringes of crystalline felodipine form I (a) SAED pattern of [211] zone axis, the highlighted spots indicate the lattice fringe that contributed to the SMFs. (b) BF-STEM image of SMFs produced by using a pixel size of 0.93 nm and 0.84 ± 0.02 nm d-spacing. From the FFT the average size of the SMFs was measured at 10.17 nm. Fourier filtered image from the area within the red box is also shown and highlights defects within the crystal. (c) Subsequent BF-STEM image of the same area showing the disappearance of the SMFs. The electron fluence in STEM for (b) and (c) was equal to 3.5 $e^-/Å^2$ and (d) 7.0 $e^-/Å^2$.

In this image, the total fluence the sample had been exposed to in STEM (at 300 kV) was approximately 43 $e^-/Å^2$, much higher than the measured C_F in CTEM at 200 kV [18].

3.4. Felodipine

Scanning moiré fringes of crystalline felodipine are shown in Figure 8, collected at a STEM magnification of 80k times, corresponding to a d_s equalling 0.93 nm. Figure 8a shows the SAED pattern of the [211] zone axis of felodipine form I. The $(11\bar{1})$ and $(\bar{1}\bar{1}1)$ crystal spacings were measured at 0.84 ± 0.02 nm and the β was equal to 1.5°.

Figure 8b shows the crystalline particle, FFT of the red highlighted area and Fourier filtered image of the same area recorded at an electron fluence of approximately 3.5 $e^-/Å^2$, slightly higher than the C_F of 2.1 $e^-/Å^2$ previously measured for felodipine at 200 kV [18]. A single spacing of 10.15 ± 0.30 nm was measured from the FFT.

The area highlighted by the blue box had previously been exposed to the electron beam in a prior scan and showed SMFs. During this previous scan (not shown), SMFs could be seen within this area with two spacings identifiable in the FFT at 7.88 ± 0.30 nm and 4.00 ± 0.30 nm. The value for the first order spacing at 7.88 ± 0.30 nm was in close agreement to the predicted value of 8.00 nm, calculated using Equation 3 when d_s, d_l and β are equal to 0.93 nm, 0.84 nm and 1.5° respectively. The increase in the size of the SMFs between the first and second scan suggests that the average size of d_l had changed between scans, possibly due to electron beam effects. The increase in SMF spacing is due to the ratio between d_s and d_l being closer to one. If d_l is equal to 0.86 nm the resulting SMFs would be 10.17 nm, an increase of 0.02 nm to the average size of d_l. The Fourier filtered image shows areas within the red box that contains lattice irregularities similar to those found in theophylline and furosemide, however, more of these defects appear to be present which could cause the average size of the SMFs to increase in this particular area.

A subsequent BF-STEM image was ac-

quired from the same area and is shown in Figure 8c. From the FFT no regular spacings were visible indicating that after a cumulative electron fluence of >7.0 $e^-/Å^2$ all signs of crystallinity were destroyed. The Fourier filtered image in Figure 7c appears to show many defects, similar to the final image for furosemide but due to the absence of spots in the FFT are due to artefacts caused by applying the spatial filter.

3.5. Discussion

The use of TEM in the pharmaceutical industry has begun to become more prominent because it can provide information at length scales not normally accessible to other techniques, identify the presence of low-levels of crystalline material and be used in the routine structural determination of small organic crystals [46, 47, 48, 49, 50]. The results here show that using the SMF method real-space lattice information can be obtained indirectly in STEM at lower magnifications than is required for direct lattice imaging, reducing the total electron fluence and damage applied to the sample. This advance opens up the ability to image the crystal lattice of electron beam sensitive organic compounds, such as those reported here for theophylline, furosemide and felodipine.

Given the low C_F of felodipine (previously measured to be 2.1 $e^-/Å^2$ at 200 kV in CTEM [18]) it would have been expected that observing fringes at electron fluences above 3.5 $e^-/Å^2$ would have been unlikely. However, SMFs were observed (Figure 8b) after exposure to an electron fluence > 3.5 $e^-/Å^2$ plus the additional fluence in CTEM (approximately < 1 $e^-/Å^2$) while searching for areas and during acquisition of SAED patterns, prior to STEM analysis. Similarly, the overall electron fluence that the furosemide particle was exposed to was approximately 6 times higher (Figure 7b and c) than the previously measured C_F in CTEM at 200 kV [18]. The increase in stability in both cases may be due to the use of 300 kV compared to 200 kV, which was previously used to determine C_F. Furthermore, C_F is only an indication of electron beam sensitivity, in this case, measured by the fading of diffraction spots. Irradiating the crystal beyond the C_F does not necessarily result in the spacings no longer being present, only that their intensity has decreased by a significant amount in the diffraction pattern.

During scanning in STEM highly localised elastic scattering events occur entirely within the area irradiated by the probe (in this case 1.4 Å in diameter) forming the SMFs. The majority of damage caused to the crystal occurs within a certain radius around the probe due to delocalised inelastic scattering, known as the point spread function [51]. The diameter depends on the size of the probe, kV and energy of the inelastic scattering event causing radiolysis. It has been estimated for 100 kV that 50% of the inelastic scattering energy occurs within a median diameter of 0.9 nm and 25 nm for energies of 10 eV and 0.1 eV respectively [51]. Provided that d_s is larger than the size of the probe and of the same order to the point spread function, the next area to be sampled in the STEM image will be from an adjacent area that has not previously been damaged from the delocalisation of radiolysis [51, 52]. If the size of d_s is closer to the probe diameter and the point spread function then damaged areas would overlap leading to damage to the crystal ahead of each dwell point. Assuming the sample indeed damages via radiolysis, which is the case for organic crystals. This

method of undersampling can be an effective way to reduce the electron fluence and damage sustained by a sample.

The disadvantage of increasing d_s (i.e. reducing the STEM magnification) is that it reduces the spatial resolution of the image. However, for beam sensitive materials the limitation in the resolution is generally a result of a low C_F and the decay in contrast due to damage. This means that C_F and the value of the initial contrast are as significant factors as the reduction in the spatial resolution. By imaging with SMFs, the lattice is magnified and additional contrast is produced from the interference between d_s and d_l, both of which increases the information content per unit specimen damage. To estimate the dose-limited resolution (DLR) for an amorphous material, several different factors are involved including the initial contrast in the image (determined by the imaging mode, sample thickness and preparation method) and the C_F, as shown in Equations 4, 5 and 6.

$$DLR = \frac{SNR\sqrt{2}}{|C|\sqrt{DQE}\sqrt{FC_F/e}} \tag{4}$$

$$where \quad F = e^{\frac{-t}{\lambda_e}} \tag{5}$$

$$and \quad C = C_0 e^{\frac{-Fluence}{C_F}} \tag{6}$$

where SNR is the signal to noise ratio which must equal or exceed some chosen background value, typically above 3 - 5 times the standard deviation to satisfy the Rose criterion [53]; DQE is the detector quantum efficiency; F is the collection efficiency of incident electrons to detected electrons (Equation 5), which depends on the sample thickness (t) and the elastic mean free path of electrons (λ_e); e is the elementary charge of an electron; C is the contrast (Equation 6) and C_0 is the initial contrast before electron beam exposure [12].

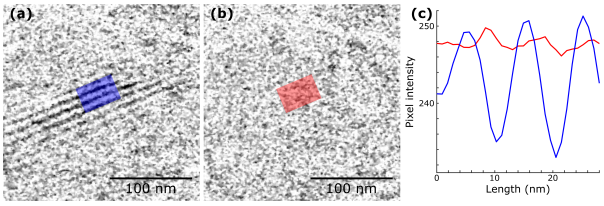

Figure 9: Processed SMF images using rolling ball background subtraction function in ImageJ and the position of the SMF line profiles. (a) Background subtracted SMF image of Figure 8b; (b) background subtracted SMF image of Figure 8c representing an amorphous sample background; (c) line profile of each coloured area in a and b showing the difference in contrast. Pixel intensity of the background was approximately 25 for each image.

When considering the DLR in BF-STEM some additional thought is required, F is decreased in BF-STEM as electrons scattered to higher angles are not collected by the BF detector, similar to the use of an objective aperture in TEM, decreasing the DLR. However, the DQE of the BF-STEM detector (a photomultiplier tube) is higher compared to a CCD [54]. Furthermore, there is no modulation transfer function in STEM as the image is recorded serially point by point, increasing the contrast and hence effective DLR in STEM. In this case the increase in DQE and contrast in STEM is assumed to cancel out the decrease in F for BF-STEM vs CTEM. Although, the samples examined here are crystalline and therefore F would not follow an exponential decay with increasing angle due to Bragg diffraction nonetheless it is instructive to assume an exponential form as a first approximation.

To ensure that the SMFs can be resolved the DLR must be smaller than the size of the fringes. SMFs introduces phase contrast into the image which can be quantified and then used as C_0 to calculate the DLR which can then be compared to an image that displays no phase contrast. The contrast is measured by determining the difference in intensities between bright and dark fringes and then dividing by the background intensity. Figure 9a and b show the background subtracted images from the raw images of felodipine in Figure 8b (phase contrast SMF image) and c (amorphous sample background exhibiting no phase contrast). A rolling ball background subtraction function in ImageJ was used; this function determines a local background value for every pixel by averaging over a very large ball around the pixel and then subtracts this from the image, effectively removing large spatial variations in the background intensities and removing the mass-thickness contrast. Line profiles taken from the same areas are shown in Figure 9c and demonstrate the contrast difference between the two scans at 3.5 $e^-/Å^2$ and 7.0 $e^-/Å^2$. When this is carried out in the same area in the image containing moiré fringes and also in the damaged image without fringes, then the average contrast values are approximately 0.6 and 0.1 respectively. Figure 10 demonstrates the effects of increasing C_0 from 0.1 to 0.6 on DLR for a fixed C_F of 2.1 $e^-/Å^2$ and when using: SNR = 5; DQE = 0.5; t = 100 nm, λ_e = 150 nm. The forms of each curve in Figure 10 shows that as the sample is irradiated with electrons there is a large initial improvement in the DLR up until a minimum at which the best resolution is achieved, in this case, 22.5 nm and 3.7 nm for C_0 of 0.1 and 0.6 respectively (note the SMF spacing was approximately 10 nm

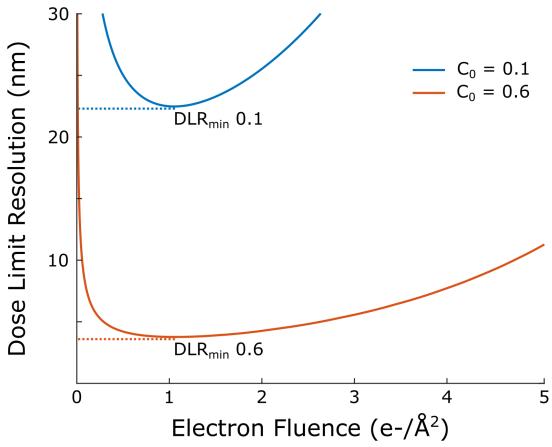

Figure 10: Plot demonstrating the effect of C_0 on the dose-limited resolution calculated by Equation 4, where SNR = 5; DQE = 0.5; t = 100 nm, λ_e = 150 nm and C_F = 2.1 $e^-/Å^2$. The minimum DLR for C_0 of 0.1 and 0.6 are 22.5 nm and 3.7 nm respectively.

in felodipine). Then as the sample is continually irradiated, damage occurs and the minimum DLR starts to deteriorate. At a C_0 of 0.6 the range of electron fluences at which the DLR is similar to the minimum DLR is larger as compared to C_0 = 0.1 due to more fluence being required to degrade the absolute contrast level and so increasing the available electron fluence at which the sample can be imaged close to the minimum DLR. Both the increase in resolution and range of electron fluences available to image the sample at higher C_0 values result in the SMFs being resolved before the sample sustains too much damage by the electron beam.

These preliminary experiments demonstrate that use of the SMF technique can increase the information content per unit specimen damage in images of the crystals by the use of SMFs. This is particularly true for beam sensitive crystals,

and the technique can be used to image a crystal lattice, identifying crystalline defects within the sample from the disruption of regular fringes. The interpretation of the precise nature of the defect is straightforward for translational moiré fringes as there is no rotational component to the interference fringes. With further development, this method could be applied to the analysis of organic crystals processed for use in medicines by the pharmaceutical industry. This opens up the possibility to investigate the impact of processing steps such as milling on the density or even type of crystalline defects This technique may also be important when dealing with recrystallisation in amorphous solid dispersions, identifying crystal nuclei and preferred growth. All these factors have an impact on the solubility and therefore bioavailability of a poorly water-soluble APIs. Further effort is required to improve the data analysis allowing more information regarding the crystal structure and defects to be extracted, for example modelling of the SMFs to predict how various defects would affect the appearance of the fringes.

4. Conclusion

In this study, the scanning moiré fringe method was used to indirectly image the crystal lattice and defects by STEM on three organic crystals highly sensitive to electron beam irradiation. The moiré patterns are produced via interference between the lattice fringes of a particular d-spacing within a crystal and the regular scan lines in STEM. This essentially causes the lattice fringes and defects that may be present in the structure to be magnified between one and two orders of magnitude, depending on the size of the original fringes and the pixel size and crucially, therefore, lowers the applied electron fluence. Increasing the size of the lattice fringes can ultimately make it possible to resolve at or inside the critical fluence for damage; increasing the information content per unit specimen damage as a result of increased contrast due to the presence of enhanced phase contrast. Disruptions to the regular SMF pattern can also indicate the presence of lattice defects or areas of amorphisation, although when the scan direction and lattice fringes are not properly aligned the orientation and position of the defect also changes making it more difficult to interpret. This technique may be applied to improve understanding of crystallisation pathways or degradation in pharmaceutical formulations.

Acknowledgements

This work was supported by the EPSRC (award number 1505716 and grant number EP/M028143/1) and AstraZeneca. The authors would like to thank Dr. Helen Blade, Dr. Leslie Hughes and Dr. Steven Cosgrove of the AstraZeneca Pharmaceutical Technology and Development Group in Macclesfield for supplying the samples of felodipine and furosemide used in the experiments and Professor Bill Jones and Dr. Mark Eddleston for supplying the theophylline sample.

References

[1] P. E. Batson, N. Dellby, O. L. Krivanek, Sub-ångstrom resolution using aberration-corrected electron optics, Nature 418 (2002) 617–620, doi:10.1038/nature00972.

[2] R. Henderson, R. M. Glaeser, Quantitative analysis of image contrast in electron micrographs of beam-sensitive crystals, Ultramicroscopy 16 (2) (1985) 139–150, doi:10.1016/0304-3991(85)90069-5.

[3] R. M. Glaeser, Limitations to significant information in biological electron microscopy as a result of radiation damage, Journal of Ultrastructure Research 36 (3-4) (1971) 466–482, doi:10.1016/S0022-5320(71)80118-1.

[4] W. Jones, M. W. Roberts, J. M. Thomas, Interaction of high-energy electrons with organic crystals in the electron microscope: Difficulties associated with the study of defects, vol. 5, The Royal Society of Chemistry, doi:10.1039/9781847556981-00065, 1976.

[5] J. F. Revol, R. S. J. Manley, Lattice imaging in polyethylene single crystals, Journal of Materials Science Letters 5 (1986) 249–251, doi:10.1007/BF01748066.

[6] S. Kumar, W. Adams, Electron beam damage in high temperature polymers, Polymer 31 (1) (1990) 15–19, doi:10.1016/0032-3861(90)90341-U.

[7] M. Pan, P. A. Crozier, Quantitative imaging and diffraction of zeolites using a slow-scan CCD camera, Ultramicroscopy 52 (3) (1993) 487–498, doi:10.1016/0304-3991(93)90065-6.

[8] Y. Pan, A. Brown, R. Brydson, Electron Beam Damage Studies on 6-Line Ferrihydrite, Journal of Physics: Conference Series 26 (1) (2006) 46, doi:10.1088/1742-6596/26/1/011.

[9] R. F. Egerton, P. Li, M. Malac, Radiation damage in the TEM and SEM, Micron 35 (6) (2004) 399–409, doi:10.1016/j.micron.2004.02.003.

[10] R. F. Egerton, Control of radiation damage in the TEM, Ultramicroscopy 127 (2013) 100–108, doi:10.1016/j.ultramic.2012.07.006.

[11] M. Hayashida, T. Kawasaki, Y. Kimura, T. Y., Estimation of suitable condition for observing copperphthalocyanine crystalline film by transmission electron microscopy, Nuclear Instruments and Methods in Physics Research B 248 (2) (2006) 273–278, doi:10.1016/j.nimb.2006.04.168.

[12] R. F. Egerton, Choice of operating voltage for a transmission electron microscope, Ultramicroscopy 145 (2014) 85–93, doi:10.1016/j.ultramic.2013.10.019.

[13] G. Siegel, Influence of very low temperature on radiation damage of organic crystals irradiated by 100 keV electrons, Z. Naturforsch 27a (2) (1972) 325–332, doi:10.1515/zna-1972-0219.

[14] R. F. Egerton, Chemical measurements of radiation damage in organic samples at and below room temperature, Ultramicroscopy 5 (1) (1980) 521–523, doi:10.1016/S0304-3991(80)80009-X.

[15] L. Reimer, J. Spruth, Interpretation of the fading of diffraction patterns from organic substances irradiated with 100 keV electrons at 10-300 K, Ultramicroscopy 10 (3) (1982) 199–210, doi:10.1016/0304-3991(82)90039-0.

[16] J. Fryer, The effect of dose rate on imaging aromatic organic crystals, Ultramicroscopy 12 (3-4) (1987) 321–327, doi:10.1016/0304-3991(87)90242-7.

[17] J. Fryer, C. McConnell, F. Zemlin, D. Dorset, Effect of temperature on radiation damage to aromatic organic molecules, Ultramicroscopy 40 (2) (1992) 3389–3398, doi:10.1016/0304-3991(92)90057-Q.

[18] M. Sari, H. Blade, R. Brydson, S. D. Cosgrove, N. Hondow, L. P. Hughes, A. Brown, Toward Developing a Predictive Approach To Assess Electron Beam Instability during Transmission Electron Microscopy of Drug Molecules, Molecular Pharmaceutics 15 (11) (2018) 5114–5123, doi:10.1021/acs.molpharmaceut.8b00693.

[19] S. J. Byard, S. L. Jackson, A. Smail, M. Bauer, D. C. Apperley, Studies on the Crystallinity of a Pharmaceutical Development Drug Substance, Journal of Pharmaceutical Sciences 94 (6) (2005) 1321–1335, doi:10.1002/jps.20328.

[20] M. Koivisto, P. Heinänen, V. P. Tanninen, V.-P. Lehto, Depth Profiling of Compression-Induced Disorders and Polymorphic Transition on Tablet Surfaces with Grazing Incidence X-ray Diffraction, Pharmaceutical Research 23 (4) (2006) 813–820, doi:10.1007/s11095-006-9785-8.

[21] M. D. Eddleston, E. G. Bithell, W. Jones, Transmission Electron Microscopy of Pharmaceutical Materials, Journal of Pharmaceutical Sciences 99 (9) (2010) 4072–4083, doi:10.1002/jps.22220.

[22] Y. Murata, J. R. Fryer, T. Baird, Molecular image of copper phthalocyanine, Journal of Microscopy 108 (3) (1976) 261–275, doi:10.1111/j.1365-2818.1976.tb01098.x.

[23] J. W. Menter, The direct study by electron microscopy of crystal lattices and their imperfections, Proceedings of the Royal Society of London A: Mathematical, Physical and Engi-

neering Sciences 236 (1204) (1956) 119–135, doi:10.1098/rspa.1956.0117.

[24] D. J. Smith, J. R. Fryer, Molecular detail in electron micrographs of quaterrylene, Nature 291, doi:10.1038/291481a0.

[25] F. Zemlin, E. Reuber, E. Beckmann, E. Zeitler, D. Dorset, Molecular resolution electron micrographs of monolamellar paraffin crystals, Science 229 (4712) (1985) 461–462, doi:10.1126/science.4012326.

[26] D. Hasa, E. Carlino, W. Jones, Polymer-Assisted Grinding, a Versatile Method for Polymorph Control of Cocrystallization, Crystal Growth & Design 16 (3) (2016) 1772–1779, doi:10.1021/acs.cgd.6b00084.

[27] J. P. Buban, Q. Ramasse, B. Gipson, N. D. Browning, H. Stahlberg, High-resolution low-dose scanning transmission electron microscopy, Journal of Electron Microscopy 59 (2) (2010) 103–112, doi:10.1093/jmicro/dfp052.

[28] A. Stevens, L. Luzi, H. Yang, L. Kovarik, B. L. Mehdi, A. Liyu, M. E. Gehm, N. D. Browning, A sub-sampled approach to extremely low-dose STEM, Applied Physics Letters 112 (4) (2018) 043104, doi:10.1063/1.5016192.

[29] E. J. Candes, J. Romberg, T. Tao, Robust uncertainty principles: exact signal reconstruction from highly incomplete frequency information, IEEE Transactions on Information Theory 52 (2) (2006) 489–509, doi:10.1109/TIT.2005.862083.

[30] D. L. Donoho, Compressed Sensing, IEEE Trans. Inf. Theor. 52 (4) (2006) 1289–1306, doi:10.1109/TIT.2006.871582.

[31] D. Su, Y. Zhu, Scanning moiré fringe imaging by scanning transmission electron microscopy, Ultramicroscopy 110 (3) (2010) 229–233, doi:10.1016/j.ultramic.2009.11.015.

[32] V. F. Holland, Dislocations in Polyethylene Single Crystals, Journal of Applied Physics 35 (11) (1964) 3235–3241, doi:10.1063/1.1713204.

[33] L. A. Bursill, J. L. Hutchison, N. Sumida, A. R. Lang, Measurements of diamond lattice displacement by platelet defects with electron microscopic moiré patterns, Nature 292 (1981) 518–520, doi:10.1038/292518a0.

[34] A. Ishizuka, M. Hytch, K. Ishizuka, STEM moiré analysis for 2D strain measurements, Microscopy 66 (3) (2017) 217–221, doi:10.1093/jmicro/dfx009.

[35] S. Kim, S. Lee, Y. Kondo, K. Lee, G. Byun, S. Lee, K. Lee, Strained hetero interfaces in Si/SiGe/SiGe/SiGe multi-layers studied by scanning moiré fringe imaging, Journal of Applied Physics 114 (5) (2013) 053518, doi:10.1063/1.4817729.

[36] S. Kim, S. Lee, Y. Oshima, Y. Kondo, E. Okunishi, N. Endo, J. Jung, G. Byun, S. Lee, K. Lee, Scanning moiré fringe imaging for quantitative strain mapping in semiconductor devices, Applied Physics Letters 102, doi:10.1063/1.4803087.

[37] Y. Murakami, T. T. Sasaki, T. Ohkubo, K. Hono, Strain measurements from $Nd_2Fe_{14}B$ grains in sintered magnets using artificial moiré fringes, Acta Materialia 101 (2015) 101–106, doi:10.1016/j.actamat.2015.08.058.

[38] A. B. Naden, K. J. OShea, D. A. MacLaren, Evaluation of crystallographic strain, rotation and defects in functional oxides by the moiré effect in scanning transmission electron microscopy, Nanotechnology 29 (16) (2018) 165704, doi:10.1088/1361-6528/aaae50.

[39] Y. Kondo, E. Okunishi, Magnified pseudo-elemental map of atomic column obtained by moiré method in scanning transmission electron microscopy, Microscopy 63 (5) (2014) 391–395, doi:10.1093/jmicro/dfu024.

[40] Y. Kondo, E. Okunishi, K.-i. Fukunage, N. Endo, Way to Reduce Electron Dose in Pseudo Atomic Column Elemental Maps by 2D STEM Moiré, Proceedings of Microscopy & Microanalysis 2017 23 (2017) 1790–1791, doi:10.1017/S1431927617009618.

[41] J. Cattle, M. S'ari, N. Hondow, P. Abellán, A. Brown, R. Brydson, Transmission electron microscopy of a model crystalline organic, theophylline, Journal of Physics: Conference Series 644 (1) (2015) 012030.

[42] J. Cattle, M. S'ari, P. Abellán, Q. Ramasse, N. Hondow, A. Brown, R. Brydson, Quantitative analysis of a model pharmaceutical material, theophylline, by transmission electron microscopy, European Microscopy Congress 2016: Proceedings (2016) 752–753doi:10.1002/9783527808465.EMC2016.6306.

[43] K. Sader, A. Brown, R. Brydson, A. Bleloch, Quantitative analysis of image contrast in phase contrast STEM for low dose imaging, Ultramicroscopy 110 (10) (2010) 1324–1331,

doi:10.1016/j.ultramic.2010.06.008.

[44] D. B. Williams, C. B. Carter, Transmission Electron Microscopy: A Textbook for Materials Science, Springer, second edn., 2009.

[45] D. T. Read, J. W. Dally, Theory of Electron Beam Moiré, Journal of research of the National Institute of Standards and Technology 101 (1) (1996) 47–67, doi:10.6028/jres.101.007.

[46] P. J. Marsac, A. C. F. Rumondor, D. E. Nivens, U. S. Kestur, L. Stanciu, L. S. Taylor, Effect of temperature and moisture on the miscibility of amorphous dispersions of felodipine and poly(vinyl pyrrolidone), Journal of Pharmaceutical Sciences 99 (1) (2010) 169–185, doi:10.1002/jps.21809.

[47] N. Li, C. J. Gilpin, L. S. Taylor, Understanding the Impact of Water on the Miscibility and Microstructure of Amorphous Solid Dispersions: An AFM-LCR and TEM-EDX Study, Molecular Pharmaceutics 14 (5) (2017) 1691–1705, doi:10.1021/acs.molpharmaceut.6b01151.

[48] V. Bhardwaj, N. S. Trasi, D. Y. Zemlyanov, L. S. Taylor, Surface area normalized dissolution to study differences in itraconazole-copovidone solid dispersions prepared by spray-drying and hot melt extrusion, International Journal of Pharmaceutics 540 (1) (2018) 106–119, doi:10.1016/j.ijpharm.2018.02.005.

[49] R. G. Ricarte, T. P. Lodge, M. A. Hillmyer, Detection of Pharmaceutical Drug Crystallites in Solid Dispersions by Transmission Electron Microscopy, Drug Development and Industrial Pharmacy 12 (3) (2015) 983–990, doi:10.1021/mp500682x.

[50] C. G. Jones, M. W. Martynowycz, J. Hattne, T. J. Fulton, B. M. Stoltz, J. A. Rodriguez, H. M. Nelson, T. Gonen, The CryoEM Method MicroED as a Powerful Tool for Small Molecule Structure Determination, ACS Central Science 4 (2018) 1587–1592, doi:10.1021/acscentsci.8b00760.

[51] R. F. Egerton, Calculation, consequences and measurement of the point spread function for low-loss inelastic scattering, Microscopy 67 (2018) i52–i59, doi:10.1093/jmicro/dfx089.

[52] R. F. Egerton, Scattering delocalization and radiation damage in STEM-EELS, Ultramicroscopy 180 (2017) 115–124, doi:10.1016/j.ultramic.2017.02.007.

[53] A. Rose, Vision - Human and Electronic, Plenum Press, doi:10.1007/978-1-4684-2037-1, 1974.

[54] A. Engel, F. Christen, B. Michel, Digital acquisition and processing of electron micrographs using a scanning transmission electron microscope, Ultramicroscopy 7 (1) (1981) 45–54, doi:10.1016/0304-3991(81)90022-X.